A Single-Cell Model of Phase-Driven Control of Ventricular Fibrillation Frequency

4 AUTHORS, INCLUDING:

Justus Anumonwo
University of Michigan
59 PUBLICATIONS **1,972** CITATIONS

SEE PROFILE

Jose Jalife
University of Michigan
150 PUBLICATIONS **6,501** CITATIONS

SEE PROFILE

A Single-Cell Model of Phase-Driven Control of Ventricular Fibrillation Frequency

Krzysztof R. Grzęda,[†‡] Justus M. B. Anumonwo,[†] Ryan O'Connell,[†] and José Jalife[†*]

[†]Department of Internal Medicine, Center for Arrhythmia Research, University of Michigan, Ann Arbor, Michigan; and [‡]Gdansk University of Technology, Gdansk, Poland

ABSTRACT   The mechanisms controlling the rotation frequency of functional reentry in ventricular fibrillation (VF) are poorly understood. It has been previously shown that Ba^{2+} at concentrations up to 50 μmol/L slows the rotation frequency in the intact guinea pig (GP) heart, suggesting a role of the inward rectifier current (I_{K1}) in the mechanism governing the VF response to Ba^{2+}. Given that other biological (e.g., sinoatrial node) and artificial systems display phase-locking behavior, we hypothesized that the mechanism for controlling the rotation frequency of a rotor by I_{K1} blockade is phase-driven, i.e., the phase shift between transmembrane current and voltage remains constant at varying levels of I_{K1} blockade. We measured whole-cell admittance in isolated GP myocytes and in transfected human embryonic kidney (HEK) cells stably expressing Kir 2.1 and 2.3 channels. The admittance phase, i.e., the phase difference between current and voltage, was plotted versus the frequency in control conditions and at 10 or 50 μmol/L Ba^{2+} (in GP heart cells) or 1 mM Ba^{2+} (in HEK cells). The horizontal distance between plots was called the "frequency shift in a single cell" and analyzed. The frequency shift in a single cell was -14.14 ± 5.71 Hz ($n = 14$) at 10 μM Ba^{2+} and -18.51 ± 4.00 Hz ($n = 10$) at 50 μM Ba^{2+}, $p < 0.05$. The values perfectly matched the Ba^{2+}-induced reduction of VF frequency observed previously in GP heart. A similar relationship was found in the computer simulations. The phase of Ba^{2+}-sensitive admittance in GP cells was -2.65 ± 0.32 rad at 10 Hz and -2.79 ± 0.26 rad at 30 Hz. In HEK cells, the phase of Ba^{2+}-sensitive admittance was 3.09 ± 0.03 rad at 10 Hz and 3.00 ± 0.17 rad at 30 Hz. We have developed a biological single-cell model of rotation-frequency control. The results show that although rotation frequency changes as a result of I_{K1} blockade, the phase difference between transmembrane current and transmembrane voltage remains constant, enabling us to quantitatively predict the change of VF frequency resulting from I_{K1} blockade, based on single-cell measurement.

INTRODUCTION

The mechanisms that control rotation frequency in reentry and ventricular fibrillation (VF) are not well understood. Recently Noujaim et al. (1) showed that increasing the inward rectifier current (I_{K1}) in a transgenic mouse model accelerates and stabilizes reentry and VF. Previously, Warren et al. (2) mapped the dominant frequency (DF) in fibrillating ventricles in the intact guinea pig (GP) heart. The investigators showed a DF gradient between ventricles, with the left ventricle fibrillating at ~30 Hz and the right ventricle at ~14 Hz. Moreover, they quantified the response of the DF in the presence of various Ba^{2+} concentrations. Specifically, in the presence of 10 or 50 μM Ba^{2+} the VF frequency dropped from 30 Hz to ~18 or 12 Hz, respectively; the higher Ba^{2+} concentration also caused VF to terminate. In a separate set of experiments in isolated GP myocytes, they showed that 10 and 50 μM Ba^{2+} blocked I_{K1} by ~15 and 60%, respectively, supporting the role of I_{K1} in controlling VF frequency. However, the mechanism by which I_{K1} affects the rotation frequency was not explored in detail.

In addition to I_{K1}, several ionic currents are known to affect VF frequency and its underlying functional reentry (rotor). The most important are I_{Kr} (3), I_{Na} (4), and I_{CaL} (5); interestingly, I_{Ks} does not seem to change significantly the frequency of reentry (6). Here, we have investigated quantitatively how electrophysiological properties at the single-cell level determine rotation frequency in two dimensions. Specifically, we endeavored to establish a link between I_{K1}-induced changes in single-cell properties and Ba^{2+}-induced changes in VF frequency in the whole heart. The rationale for focusing on I_{K1} was based on its strong and well established effect on the VF frequency and its fast (almost instantaneous) kinetics, which obviates the need to consider accumulation and complicated transitions between states. The motivation for this study derived from analysis of reentry behavior in an idealized 2D mathematical monodomain model, described by the equation

$$i_{ion}(x,y,t) + \frac{\partial V_m(x,y,t)}{\partial t} = D \times \frac{\partial^2 V_m(x,y,t)}{\partial x^2} + D \times \frac{\partial^2 V_m(x,y,t)}{\partial y^2}, \quad (1)$$

where V_m is the transmembrane voltage, i_{ion} is the total ionic current normalized to membrane capacitance, and D is the diffusion coefficient. It is easy to show that at least in an ideal, continuous, infinite, homogenous, and isotropic system, if some solution $V_m(x,y,t), i_{ion}(x,y,t)$ satisfies Eq. 1, then $\widehat{V}_m(x,y,t) = V_m(ax,ay,t), \widehat{i}_{ion}(x,y,t) = i_{ion}(ax,ay,t)$ satisfies the equation

$$\hat{i}_{\mathrm{ion}}(x,y,t) + \frac{\partial \hat{V}_m(x,y,t)}{\partial t} = \frac{D}{a^2} \times \frac{\partial^2 \hat{V}_m(x,y,t)}{\partial x^2} + \frac{D}{a^2} \times \frac{\partial^2 \hat{V}_m(x,y,t)}{\partial y^2}. \quad (2)$$

In other words, at least in an idealized case, changes in diffusion coefficient D only stretch the solution in space, without affecting its time properties (like frequency). Consequently, the periodicity of the solution in the time domain would be determined by the ionic properties, i.e., the modeling details of i_{ion}.

The second premise for our hypothesis comes from many biological and artificial systems displaying phase-locking behavior [7–11]. Anumonwo et al. [7] observed a phase-resetting phenomenon in rabbit sinoatrial node. In particular, they showed that subthreshold electrotonic current (perturbation) applied to a spontaneously discharging cell was able to modulate the cell behavior depending on the phase of the applied perturbation. Under certain conditions, the applied perturbation created phase-locking behavior, bringing the cell's discharge frequency to the perturbation frequency and keeping a constant phase difference between the current disturbance and the action potential. Subthreshold interactions between oscillators have also been described in other biological systems [11]. Also, artificial oscillating systems (e.g., the phase-lock loop circuit [8]) are capable of responding by frequency and/or phase change in a manner proportional to the phase of the perturbation. Those observations prompted us to hypothesize that although the rotation frequency is changing due to I_{K1} modulation, the phase of whole-cell admittance tends to remain constant.

METHODS

Solutions

Whole-cell recording

Cardiac myocyte solutions. *Ca^{2+}-free cardioplegic solution* (mM): 280 glucose, 13.44 KCl, 12.6 NaHCO$_3$, and 34 mannitol.

Tyrode's solution (mM): 148 NaCl, 5.4 KCl, 1.0 MgCl$_2$, 1.8 CaCl$_2$, 0.4 NaH$_2$PO$_4$, 5.5 glucose, and 15 HEPES, pH 7.4 (NaOH).

Low-Ca^{2+} solution: 148 mM NaCl, 5.4 mM KCl, 1.0 mM MgCl$_2$, 0.4 mM NaH$_2$PO$_4$, 5.5 mM glucose, 15 mM HEPES, and 1 mg/mL albumin, pH 7.2 (NaOH).

Enzyme solution: This solution was similar to the low-Ca^{2+} solution, with the addition of 100 units/mL collagenase (type II, Worthington, Lakewood, NJ).

KB solution (mM): 80 KCl, 5 MgSO$_4$, 30 KH$_2$PO$_4$, 20 glucose, 0.25 EGTA, 5 creatine, 5 β-hydroxybutyric acid, 20 taurine, 5 pyruvic acid, and 5 ATP, pH 7.4 (KOH).

Pipette solution (mM): 119 KCl, 5 NaCl, 5 K$_2$ATP, 10 HEPES, 1 MgCl$_2$, and 10 EGTA;, pH 7.2 (KOH).

HEK cells. *Tyrode's solution* (mM): 140 NaCl, 5.4 KCl, 1.8 CaCl$_2$, 0.33 NaH$_2$PO$_4$, and 5.0 HEPES, pH 7.4 (NaOH).

Pipette solution (mM): 148 KCl, 1 MgCl$_2$, 5 EGTA, 5 HEPES, 2 creatine, 5 ATP, and 5 phosphocreatine, pH 7.2 (KOH) [13].

Isolation of myocytes

The Langendoff retrograde perfusion method was used to isolate GP ventricular cells, as described previously [12–14]. The protocol was consistent with the National Institutes of Health guidelines (NIH publication no. 85-23, revised 1996). Briefly, guinea pigs were first heparinized and then anesthetized with sodium pentobarbital. After thoracotomy, the heart was immediately removed and retrogradely perfused with Tyrode's solution (37°C) to clear excess blood. This was followed by perfusion with Ca^{2+}-free solution for 10 min, then enzyme solution for 15 min, then recovery/storage solution (KB medium) for 10 min. Cells were obtained by mechanically teasing apart sections of the left ventricle only. Isolated cells were kept at 37°C in the KB solution for another 30 min before a stepwise reintroduction of Ca^{2+}. Cells were kept at room temperature until the beginning of electrophysiological recordings.

Cell culture

Cell culture procedures were carried out as previously described [13,15]. The procedure for the generation of the double (Kir2.1/Kir2.3) stably transfected cell lines has been described previously [15]. Briefly, HEK cells were transfected using Effectene (Qiagen, Valencia, CA). A stable Kir2.3 cell line was generated using plasmids containing pcDNA3 vector. The Kir2.1/Kir2.3 double stables were generated by transfecting Kir2.1 (pcEP4 vector) into the stable Kir2.3 HEK cells followed by selection with hygromycin and neomycin. The colonies stably expressing the resistance marker were selected.

Electrophysiology

Electrophysiological recordings were carried out at 35°C in the whole-cell configuration using the Multiclamp 700B amplifier and Clampex 9.0 software (Molecular Devices, Foster City, CA). Series resistance compensation (correction of up to 80%) was implemented in all experiments. The holding potential (HP) was −80 mV and a series of voltage-clamp sinusoidal trains was generated and applied to the cells. The protocol was generated using a custom macro developed in Microsoft Excel (Microsoft, Redmond, WA). Briefly, the applied protocol was composed of a sinusoidal signal of 15 mV amplitude and DC offset (V_{DC}) of −35 mV in GP left ventricular cells and −25 mV in HEK cells; thus the command voltage ranged between −50 and −20 mV in GP myocytes and −40 and −10 mV in HEK cells (liquid junction potential not corrected). These voltage values were chosen to match the region of negative slope in I/V relationships in these cell types. The frequency of the sinusoidal wave was increased from 5 to 50 Hz in 5-Hz steps. Each frequency was applied for 5 s and between subsequent frequencies, holding voltage was applied for 4 s to allow for cell recovery. Immediately before and after the frequency sweep, a ramp protocol was applied to verify the viability of the cell; only viable cells were selected for analysis.

The use of sinusoidal command voltages was motivated by two factors. First, a sinusoidal voltage signal contains only one frequency, whereas spectra of other signals (like square pulses) would contain in addition many/infinite numbers of harmonics. Thus, using the sinusoidal protocol was beneficial, since one of the aims of this study was to investigate the mechanism controlling the frequency of reentry. Second, as shown below, we performed 2D simulations that suggested that the sinusoidal voltage reasonably approximated conditions in the reentry core. For the same reason, i.e., an attempt to reproduce core conditions, we selected the command voltage range for voltage clamp in GP myocytes. As shown later in the simulation, the voltage within the core did not seem to drop below −74 mV (which corresponded to the peak I_{K1} in the model). Since there is no perfect match between the I_{K1} I/V relationship in the model and in the GP cell, we defined the voltage range for the patch-clamp experiments based on the I_{K1} function (i.e., to match the negative slope of the I/V relationship) rather than on the absolute voltage range. A similar justification was used for the HEK cells.

Each cell was subjected to the described protocol in control conditions and in the presence of Ba^{2+} (10 and/or 50 μM for GP cells and 1 mM for HEK cells). The concentration used in HEK cells was intended to block I_{K1} completely, so that we could investigate the contribution of I_{K1} to the

whole-cell admittance. In GP myocytes, on the other hand, we limited our range of concentrations to ~50 μM or lower based on a previous study by Warren et al. (2) showing that concentrations exceeding this range were sufficient to terminate VF. Full blockade of I_{K1} in the GP cells would not be useful, since 50 μM Ba^{2+} (which blocks I_{K1} partially) is sufficient to terminate VF in the GP heart.

Analysis

We selected a 1-s segment (from 3.5 to 4.5 s of the sinusoidal burst) of the current response and voltage stimulation for each voltage frequency and amplitude. The initial 3.5-s segment was ignored to avoid transient effects on the admittance measurements, and the final 0.5 s was discarded to ensure that an integer number of sinusoidal cycles was analyzed. The components at the given fundamental frequency were selected from both signals and appropriately divided to obtain the admittance (for more details on the concept of admittance, see Chen (16)). Formally, we calculated the complex representation of the transmembrane (command) voltage as

$$V(f) = 2\frac{1}{\Delta t f_s} \sum_{n=t_1 f_s + 1}^{\Delta t} \exp\left(j\frac{2\pi f}{f_s}n\right) V_m[n],$$

where $V(f)$ is a complex representation of the voltage at frequency f, $\Delta t = 1$ s is the length of the segment selected for analysis, $t_1 = 3.5$ s is the location of the segment relative to the beginning of the sinusoidal burst, $f_s = 1$ kHz is the sampling frequency, and $V_m[n]$ is the series of voltage samples. In an analogous manner, we calculated the complex representation of the transmembrane current as

$$I(f) = 2\frac{1}{\Delta t f_s} \sum_{n=t_1 f_s + 1}^{\Delta t} \exp\left(j\frac{2\pi f}{f_s}n\right) i_m[n],$$

where $I(f)$ is a complex representation of the membrane current at frequency f and $i_m[n]$ is the series of current samples. The algorithm is equivalent to calculating the Fourier transform of the selected signal block and picking its value at frequency f. Afterward, we calculated "raw" admittance as

$$Y_{\text{raw}}(f) = \frac{I(f)}{V(f)}.$$

Since the digitizer does not sample all channels at the same time, but rather introduces delay between samples acquired from different input channels, the raw admittance was then corrected for that sampling delay and for the uncompensated portion of the series resistance:

$$\frac{1}{Y(f)} = \frac{1}{Y_{\text{raw}}(f)\exp\left(-j2\pi\frac{\Delta n f}{f_s}\right)} - (1-\eta)R_s,$$

where Δn is the sampling delay between voltage and current (in samples), R_s is the series resistance, and η is the degree of series-resistance compensation (i.e., 0.8 for 80% compensation, etc.). The protocol timing resulted from a trade-off between our desire to achieve steady-state measurement and the ability of the cells to survive the protocol.

Single-cell simulations

A series of computer simulations of a single cell was also performed. Ionic currents were modeled using the Luo-Rudy (LR2000) model (17,18). Calcium release from the sarcoplasmic reticulum was programmed to be triggered by a voltage increase above the level of -35 mV unless specified otherwise. In each simulation, a sinusoidal voltage of the same frequency, amplitude, and DC offset as in patch-clamp experiments was applied to the model cell. The transmembrane current (the sum of all ionic currents and the capacitative current) was taken from the simulation as the current response and analyzed. We used previously described custom simulation software (19); the integration step was 10 μs.

The I_{K1} current was formulated as

$$i_{K1} = G_{K1} \times \left(\frac{[K^+]_o}{5.4 \text{ mM}}\right)^{1/2} \times K1 \times (V_m - E_{K1}),$$

$$\alpha = \frac{1.02}{1 + \exp(0.2385 \times (V_m - E_{K1} - 59.215 \text{ mV}))},$$

$$\beta = \frac{0.49124 \times \exp(0.08032 \times (V_m - E_{K1} + 5.476)) + \exp(0.06175 \times (V_m - E_{K1} - 594.31))}{1 + \exp(-0.5143 \times (V_m - E_{K1} + 4.753))},$$

$$K1_\infty = \frac{\alpha}{\alpha + \beta}.$$

G_{K1} was assumed to be either 0.75 or 1.125 $\text{mS} \cdot \mu F^{-1}$, corresponding to $I_{K1\text{peak}} = 3.0$ pA/pF or $I_{K1\text{peak}} = 4.5$ pA/pF, respectively. In both cases, peak I_{K1} occurred at $V_m = -74$ mV.

The current was assumed to be time-independent, i.e., $K1 = K1_\infty$, unless otherwise specified. In the simulations with time-dependent I_{K1}, $K1$ was determined by the differential equation

$$\frac{dK1}{dt} = \frac{K1_\infty - K1}{\tau_{K1}}$$

with a fixed, voltage-independent time constant τ_{K1}.

2D simulations

We simulated a 2D domain composed of 200×200 nodes, aligned in a square grid at 0.1 mm node-to-node distance. Each node was assigned a capacitance of 153.4 pF, and the internodal conductance was set to 0.00024 mS. Euler's integration scheme was used with a time step of 100 μs and analytical expressions for updating of gating variables. Using the cross-field stimulation protocol, stable reentry was initiated and its rotation frequency was measured.

Statistical analyses

Data are presented as the mean $\pm$ SD. When phases of complex numbers are presented, the phase of the mean is given; the standard deviation was calculated from complex numbers divided over their moduli to normalize. Comparisons were made using the two-tailed t-test; $p < 0.05$ was regarded as statistically significant.

RESULTS

Computer simulations

2D reentry

We carried out computer simulations to directly test our hypothesis that whereas the rotation frequency changes during Ba^{2+} application, the phase of whole-cell admittance remains constant, and also to establish appropriate conditions for subsequent experiments. We performed 2D simulations using LR2000 kinetics with two levels of I_{K1} expression: peak I_{K1} at either 3.0 or 4.5 pA/pF. Using cross-field stimulation, we obtained a stable reentry rotating at dominant frequencies of 11.72 Hz at $I_{K1peak} = 4.5$ pA/pF and 10.55 Hz at $I_{K1peak} = 3.0$ pA/pF. Thus, reduction of I_{K1} "down-shifted" the reentry frequency by 1.17 Hz ($\Delta f_{rotor} = -1.17$ Hz). This result is not surprising given the role of I_{K1} in controlling rotation frequency (1,20).

In Fig. 1, we present a snapshot from the control simulation of sustained reentry. Fig. 1 A shows the map of transmembrane voltage V_m distribution around the center of rotation. In Fig. 1 B, we plotted voltage profiles around the center at different distances. The voltage profile around the core (five nodes from the singularity point; *blue line*) can be reasonably described as sinusoidal. In an analogous way, Fig. 1 C shows the map of the radial current around the rotation center, that is, the electrotonic current that flows from cell to cell away from the center of rotation. In Fig. 1 D, we plotted profiles of this current around the center. Here, also, current profile at a distance of five nodes from the singularity point (*blue line*) can be reasonably approximated by a sinusoid.

To find the center of rotation, we generated a phase movie from each simulation and identified the phase singularity as the center of rotation. We confirmed that voltage amplitude at that point remained low during the analysis time frame. Fig. 1 E shows the voltage trace recorded in the center of rotation. As can be seen, the voltage stays in the narrow band until ~8 s from the simulation onset, when the reentry loses stability because of intracellular calcium displacement (model artifact; data not shown). Furthermore, Fig. 1 F
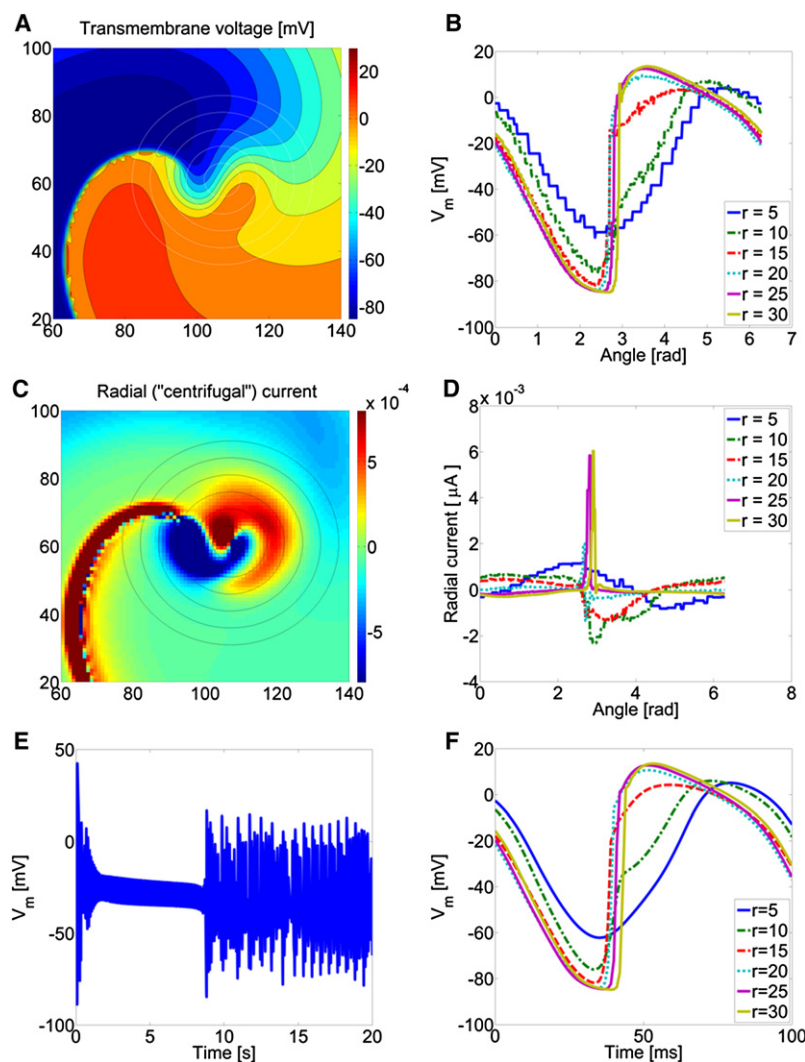

FIGURE 1 Snapshot from 2D simulation with control LR2000 kinetics. (A) Transmembrane voltage map. Circles are 5–30 nodes from the center of rotation in 5-node increments. (B) Voltage profiles around the rotation center. r, distance from the rotation center. (C) Map of the radial ("centrifugal") component of current. (D) Profiles of centrifugal current around the rotation center. r, distance from the rotation center. (E) Voltage recorded in the center of reentry rotation. The voltage stays within an ~20-mV band until 8 s after the simulation starts, which confirms the stability of reentry during this timeframe. (F) Voltage courses at several distances from the center. Horizontal axis is scaled in milliseconds from an arbitrary selected beginning of the cycle.
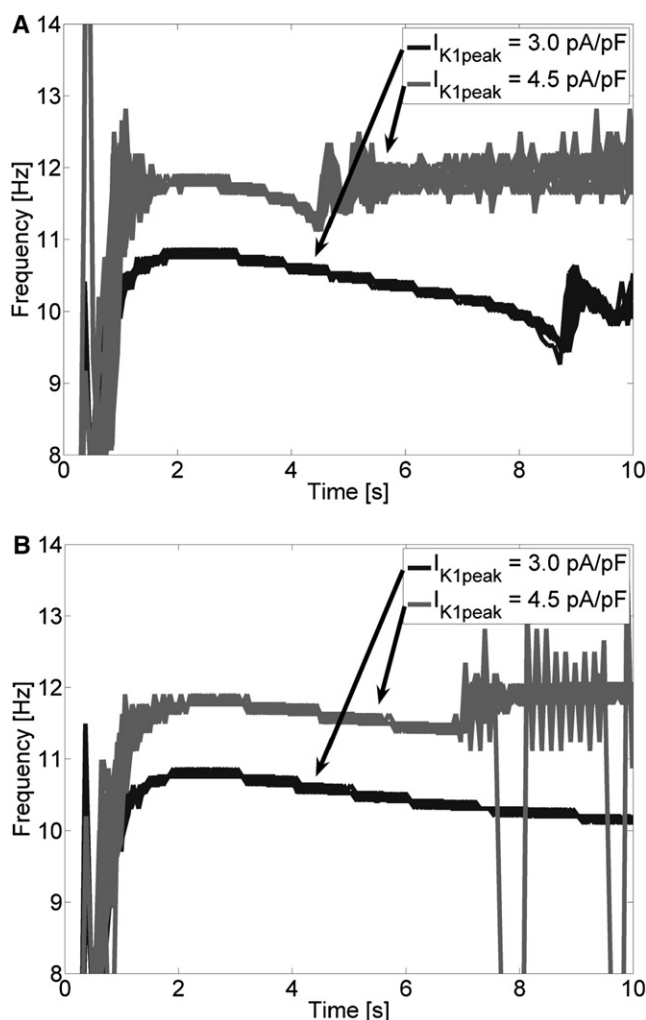
FIGURE 2 Frequency in the 2D simulations (with $I_{K1peak} = 3.0 \, pA/pF$ and $I_{K1peak} = 4.5 pA/pF$) as a function of time, recorded at 16 points uniformly spaced over the 2D sheet (superimposed). (A) Original LR2000 model; the frequency decays slowly until loss of stability at 8.5 or 4.5 s. (B) Calcium release threshold in the model adjusted to -30 mV delays intracellular calcium displacement and makes the reentry stable for longer times. Please note that in both model versions the frequency change follows the same pattern.

confirms that at the specified distances, the voltage traces in the time domain (Fig. 1 E) and around the core (Fig. 1 B) are of the same shape, which confirms the stability of the reentry. In Movies S1 (for $I_{K1peak} = 3.0 \, pA/pF$) and S2 (for $I_{K1peak} = 4.5 \, pA/pF$) of the Supporting Materials, we present the voltage maps from two different 2D reentry simulations to confirm the periodicity of the reentry.

Frequency was determined on a beat-to-beat basis (as the inverse of cycle length) from 16 points that were uniformly spaced over the simulated 2D sheet. The instantaneous frequency is shown in Fig. 2 at two different levels of I_{K1peak}. In the original LR2000 model, the frequency decays slowly until the reentry loses stability due to intracellular calcium displacement (please see also Fig. 1 E). Adjusting the calcium release threshold to -30 mV prolonged the stability of the reentry. In Table 1, we present the activation frequency averaged over all 16 points in the time window of 2.0–4.5 s (i.e., before stability was lost). For comparison, we present, in the same table, the dominant frequency calculated by power spectral analysis. Because both frequency plots follow a similar decay pattern, comparison between their averages is justified.

Single cell

We simulated in silico a voltage-clamp experiment to measure cell admittance. The same cellular model of kinetics as in the 2D reentry simulation (with two levels of I_{K1} expression) was used. We determined the temporal relationship between current and voltage using the protocol depicted in Fig. 3 (see also Methods). We then plotted the admittance phase as a function of frequency and determined the frequency shift in a single cell (Δf_{cell}), as shown in Fig. 4 A. The frequency shift caused in the LR2000 model by reduction of the I_{K1peak} from 4.5 to 3.0 pA/pF was -1.24 Hz, which was close to the frequency shift in 2D reentry.

Sensitivity

To test for sensitivity of the results to model parameters, we performed an additional set of simulations. In these new scenarios, two different values of I_{K1} expression levels were applied on a background of different changes to the ionic model, as shown in Table 1. Moreover, we conducted simulations to determine the sensitivity of the admittance measurement over the voltage range between -60 and

shows the voltage traces recorded during one cycle of reentry rotation at several points, each located at a specified distance away from the center of rotation. Comparison with Fig. 1 B

TABLE 1 Effect of I_{K1} modulation in different model variations

Background model change	Frequency at $I_{K1peak} = 3.0 \, pA/pF$		Frequency at $I_{K1peak} = 4.5 \, pA/pF$		Δf_{cell} (Hz)	Δf_{rotor}		$\frac{\Delta f_{rotor}}{\Delta f_{cell}}$ (TD)
	TD (Hz)	DF (Hz)	TD (Hz)	DF (Hz)		TD (Hz)	DF (Hz)	
Base	10.71	10.55	11.66	11.72	$-1.15/-1.11$	-0.94	-1.17	0.82/0.85
I_{Ks} (2×)	12.32	12.50	14.06	14.06	$-1.60/-1.92$	-1.75	-1.56	1.09/0.91
I_{Kr} (2×)	11.54	11.72	12.94	12.89	$-1.30/-1.30$	-1.40	-1.17	1.08/1.08
I_{NACa} (1.5×)	10.01	10.16	11.22	11.33	$-1.06/-1.01$	-1.21	-1.17	1.14/1.20
I_{CaP} (1.2×)	10.91	10.94	11.87	11.72	$-1.12/-1.09$	-0.95	-0.78	0.85/0.88
-30 mV	10.72	10.55	11.74	11.72	$-1.19/-1.22$	-1.02	-1.17	0.86/0.83

The single-cell frequency shift, Δf_{cell}, and the $\frac{\Delta f_{rotor}}{\Delta f_{cell}}$ ratio are given for the test voltage ranges -50 to -20 mV and -60 to 0 mV, respectively. DF, dominant frequency; TD, frequency obtained in the time domain.
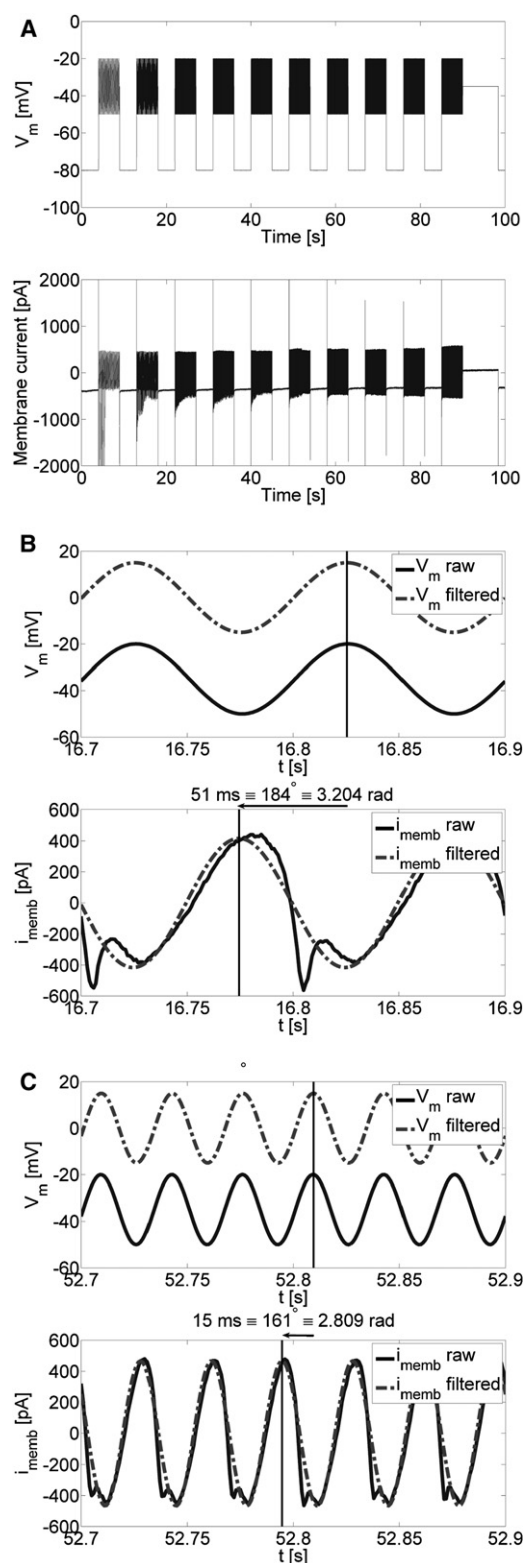
A

B

C

FIGURE 3 Admittance measurements in single guinea pig ventricular myocytes. (*A*) Sinusoidal voltage-clamp protocol showing command voltage applied to the cell (*upper*) and the recorded current (*lower*). (*B* and *C*) Zoomed-in portions of the protocol, with frequencies of 10 and 30 Hz, respectively, applied. The solid lines show recordings of the raw command voltage applied to the cell (*upper*) and the whole-cell current (*lower*). The

0 mV. The parameter being analyzed ($\frac{\Delta f_{\mathrm{rotor}}}{\Delta f_{\mathrm{cell}}}$) stayed within $\pm 20\%$ of 1.

Cellular electrophysiology

Frequency shift in isolated guinea pig myocytes

To determine the role of I_{K1} in determining rotation frequency in the control, we analyzed Ba^{2+}-sensitive whole-cell admittance in left ventricular GP myocytes in voltage-clamp experiments, based on our simulation results. For each cell, we applied the protocol depicted in Fig. 3, *A–C*. We then calculated whole-cell admittances and plotted the family of admittance-phase characteristics as a function of frequency for different barium concentrations (Fig. 4 *B*). Next, we determined the admittance phase at 30 Hz in control conditions (2.44 rad $= 140°$ in the example presented in the figure), and then the frequency that gave the same phase in the presence of 10 μM Ba^{2+} (17.82 Hz in the example). The frequency difference, $\Delta f_{\mathrm{cell}} = -12.18$ Hz, referred to as the "frequency shift", was then taken for statistical analysis. In Fig. 4 *C*, we show the average frequency shift, Δf_{cell}, in single cells as a function of the Ba^{2+} concentration (*bars*): Δf_{cell} was -14.14 ± 5.71 Hz ($n = 14$) for 10 μM Ba^{2+} and -18.51 ± 4.00 Hz ($n = 10$) for 50 μM Ba^{2+}, $p < .05$. For comparison, the crosses show the effect of the respective Ba^{2+} concentrations on VF frequency in intact hearts, reported previously in the literature (2).

Barium-sensitive admittance: the role of I_{K1}

To analyze the effects of Ba^{2+} on whole-cell admittance in more detail, we focused on two frequencies: 10 Hz (the rotation frequency in the 2D computer model) and 30 Hz (the VF frequency in the intact GP heart (2)). In Fig. 5, we present sample vector graphs for one cardiomyocyte. Fig. 5, *A* and *B*, shows data at 10 and 30 Hz, respectively. In this type of graph, the length of each vector represents the magnitude of the admittance (i.e., the ratio between current amplitude and voltage amplitude), whereas the direction (angle) of each vector represents the phase of the admittance (i.e., the phase shift between current and voltage). Vectors drawn with solid and dashed lines denote true admittance measured in the presence of 0 and 50 μM Ba^{2+}, respectively. The vectorial difference between admittances observed in control conditions and in the presence of Ba^{2+} was called "Ba^{2+}-sensitive admittance", plotted as dotted vectors and taken for further analysis.

Fig. 5 *C* shows a vector graph for whole-cell Ba^{2+}-sensitive admittance at 10 and 30 Hz, measured in GP myocytes (average and standard deviation of dotted vectors from Fig. 5, *A* and *B*). It was surprising to see that in GP

dashed lines show the voltage and current signals resulting from digital processing (filtering at 10 and 30 Hz, respectively). The current is advanced by 51 (*B*) and 15 ms (*C*) with respect to the voltage, corresponding to raw admittance phases of 3.204 rad at 10 Hz and 2.809 rad at 30 Hz, respectively.
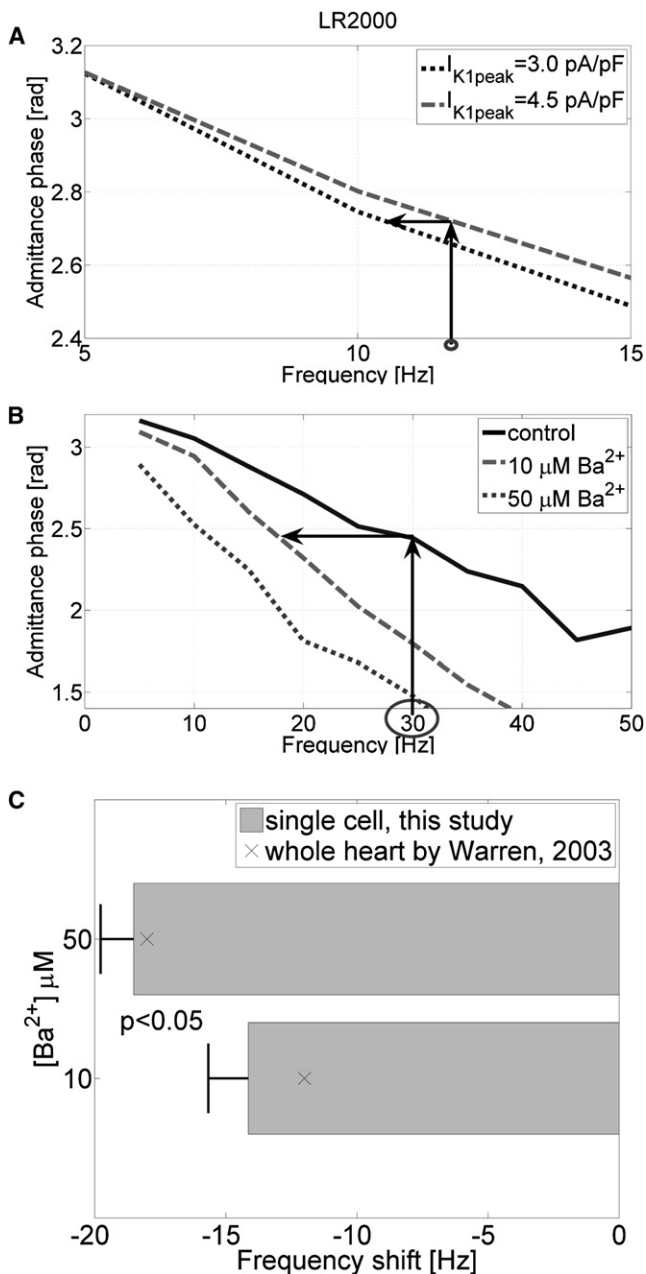
LR2000

FIGURE 4 (A) Admittance phase versus frequency plots for the LR2000 model and graphic depiction of the "frequency shift", Δf_{cell}, in single cells. Dotted line shows data at $I_{K1peak} = 3.0$ pA/pF; dashed line at $I_{K1peak} = 4.5$ pA/pF. Originating from a frequency of 11.72 Hz (*circle on the frequency axis*), which is the reentry frequency at $I_{K1peak} = 4.5$ pA/pF, we find an admittance phase equal to 2.72 rad (*vertical arrow*). At $I_{K1peak} = 3.0$ pA/pF, the same value of admittance phase is reached at a frequency lower by 1.24 Hz (*left-pointing arrow*). Thus, we find the frequency shift in a single cell, Δf_{cell}, equal to −1.24 Hz. (B) Admittance phase versus frequency plots for one guinea pig left ventricular myocyte and graphic depiction of VF frequency prediction from single-cell measurements. Originating from a frequency of 30 Hz (*circle on the frequency axis*), which represents VF in control conditions, we find an admittance phase equal to 2.44 rad. In the presence of 10 μM Ba^{2+}, the same value of admittance phase is reached at a frequency lower by 12 Hz (*left-pointing arrow*). Thus, we find the frequency shift in this cell, Δf_{cell}, equal to −12 Hz. (C) Comparison between frequency shift as a function of Ba^{2+} concentration

cardiomyocytes, not only the whole-cell admittance but also its Ba^{2+}-sensitive component (at 50 μM) has a substantial imaginary part; the phase of Ba^{2+}-sensitive whole-cell admittance was −2.65 ± 0.32 rad at 10 Hz and −2.79 ± 0.26 rad at 30 Hz. Assuming near instantaneous gating of I_{K1}, and given that it has a region of negative I/V slope over the voltage range being applied, we might expect that Ba^{2+}-sensitive admittance should have a significant, negative real part and an imaginary part equal to 0, yielding an admittance phase of $\pm\pi$ rad. Thus, the admittance deviated substantially from the theoretical expectation based on I_{K1} properties. In Fig. 6, A and B, the frequency dependence of the real and imaginary parts of admittance predicted by the simulation using the LR2000 model (Fig. 6 A) is compared with that demonstrated experimentally for a GP myocyte (Fig. 6 B). In the model, the "Ba^{2+}-sensitive" admittance is purely real, with the imaginary part equal to 0, as plots of the imaginary part for 3.0 and 4.5 pA/pF peak I_{K1} levels perfectly superimpose in Fig. 6 A (*upper graph*). The latter is not surprising, given that I_{K1} is modeled as an instantaneous current in the LR2000 model. Hence, when the transmembrane voltage changes, I_{K1} changes immediately, with zero delay. Moreover, in the plot of the real part of admittance (Fig. 6 A, *lower graph*), the difference between the two different I_{K1} expression levels does not change at any level of frequency. In contrast, Fig. 6 B demonstrates that the experimentally measured Ba^{2+}-sensitive admittance is frequency-dependent for both real and imaginary parts in control and at each Ba^{2+} concentration tested, which implies that factors in addition to I_{K1} are modifying the admittance property of the myocyte.

To investigate the apparent discrepancy between GP myocytes and model predictions, we performed experiments in HEK cells heterologously coexpressing Kir2.1/2.3 channels, which are major components of I_{K1} in GP ventricles (13). Fig. 7 A (constructed analogously to Fig. 5 C) shows that in HEK cells, the Ba^{2+}-sensitive admittance deviates only slightly from the real axis; the phase of Ba^{2+}-sensitive whole-cell admittance was 3.09 ± 0.03 rad at 10 Hz and 3.00 ± 0.17 rad at 30 Hz; i.e., with phase values that were slightly lower than π rad and that decreased with increasing frequency. In Fig. 7, B and C, we present the average characteristics of Ba^{2+}-sensitive admittance in HEK cells as a function of frequency, with the imaginary and real parts of admittance (Fig. 7 B, *upper and lower*, respectively), and the argument (phase) of admittance (Fig. 7 C). Admittance was measured in control conditions (*solid line*) and in the presence of 1 mM Ba^{2+} (*dashed line*). In HEK cells, we could use such a high Ba^{2+} concentration to block I_{K1} completely, whereas in GP we were limited to a range of

in single cells (*solid bars*; please note that the error bars indicate standard errors, not standard deviations) versus the reference frequency shift in intact guinea pig heart measured by Warren et al. (2003) (*crosses*; note: Warren's measurements were made at 3 and 12.5 μM Ba^{2+}, not exactly at 10 μM).
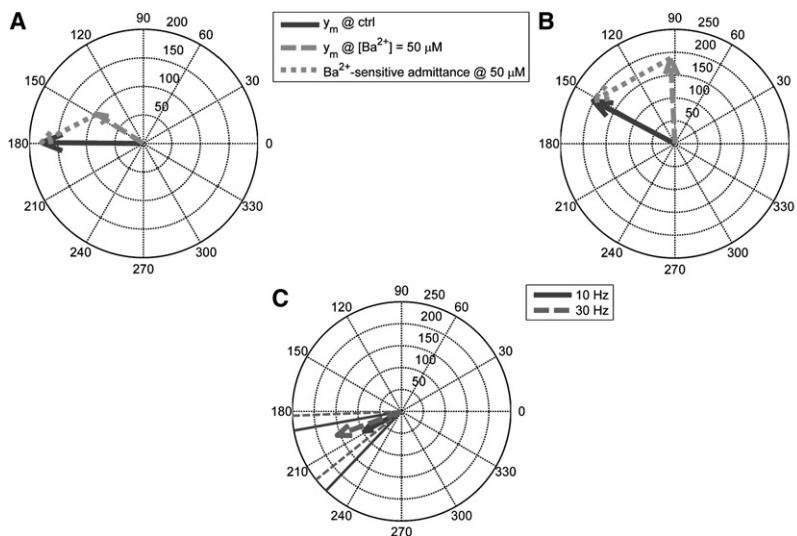
FIGURE 5 Vector plots of whole-cell admittance (normalized to the cell capacitance and expressed in S/F) at two frequencies in a sample guinea pig left ventricular cell. (A) Data for 10 Hz. (B) Data for 30 Hz. The length of each vector represents the magnitude of the admittance (i.e., the ratio between current amplitude and voltage amplitude), whereas the direction (angle) of each vector represents the phase of the admittance (i.e., the phase shift between current and voltage). Vectors drawn with solid and dashed lines denote true admittance measured in the presence of 0 and 50 μM Ba^{2+}, respectively. Dotted vectors are plots representing "Ba^{2+}-sensitive admittance," i.e., vectorial differences between admittances observed in control conditions and in the presence of barium. (C) Whole-cell Ba^{2+}-sensitive mean (average of the dotted vectors in A and B) admittance in one GP cell at 50 μM Ba^{2+}. Solid radii denote the standard deviation calculated from admittances normalized to their magnitudes.

concentrations that were selective for I_{K1} blockade ($\leq 50\ \mu$M) and used previously to terminate VF (2). Next, the Ba^{2+}-sensitive admittance (*dotted line*) was calculated as the vectorial difference between the control and 1 mM Ba^{2+}. Whereas the real part is approximately -225 S/F at all frequencies, the imaginary part seems to increase linearly with frequency at a rate of ~1.25 S/F/Hz. In other words, Ba^{2+}-sensitive admittance, normalized to cell capacitance, equals $Y(f) = -225\ \text{S} \cdot \text{F}^{-1} + j \times 2\pi f \times \frac{1.25\ \text{S} \cdot \text{F}^{-1} \cdot \text{Hz}^{-1}}{2\pi}$. From the basic circuit analysis, the real part of -225 S/F would correspond to the negative slope in the I_{K1} I/V relationship of the order of $-0.225 \frac{\text{pA/pF}}{\text{mV}} = \frac{-6.75\ \text{pA/pF}}{30\ \text{mV}}$.

Similarly, the product $\left| \frac{1.25\ \text{S} \cdot \text{F}^{-1} \cdot \text{Hz}^{-1}}{2\pi} \times \frac{1}{-225\ \text{S} \cdot \text{F}^{-1}} \right| \approx 0.88$ ms would approximate the time constant of the Ba^{2+}-sensitive current.

To test the hypothesis that the observed discrepancy is due to the time dependence of I_{K1}, we performed additional simulations of admittance measurements in the single-cell model after incorporating time-dependence into I_{K1}. We used I_{K1} from the simulation as the equivalent of Ba^{2+}-sensitive current. Consequently, the admittance related to I_{K1} (denoted as Y_{K1}) was a model equivalent of Ba^{2+}-sensitive admittance measured in the patch-clamp experiments. In Fig. 8, we present the characteristics of the I_{K1} admittance as a function of frequency, obtained for two different values of the I_{K1} time constant (τ_{K1}), namely 0.8 ms and 2.0 ms, and for the time-independent I_{K1} as the control. These simulations were equivalent to HEK measurements, and the peak I_{K1} in the model was equal to 15.45 pA/pF.

Clearly, the assumption of $\tau_{K1} = 0.8$ ms yields characteristics similar to those observed in HEK cells (see Fig. 7 for comparison), i.e., with admittance phase at 50 Hz equal to 2.84 rad, admittance real part ranging from -225 to -210 S/F over the frequency range from 5 to 50 Hz, and admittance imaginary part slope of the order of 1.21 S/F/Hz.

The remaining difference (in HEK cells, the real part of the Ba^{2+}-sensitive admittance does not tend toward zero in Fig. 7 B) could be attributed to complex behavior of the channel population in the presence of a changing electrical field, which could not be observed when data for modeling were acquired using step or ramp voltage-clamp protocols.

To quantitatively compare the current traces recorded in GP and HEK cells, we also calculated the levels of the second and third harmonics in barium-sensitive current, applying the same method previously used to detect the current amplitude at the test (fundamental) frequency. The levels of harmonics were normalized to the signal level at fundamental frequency. The values are presented in Table 2. The harmonics amplitudes differ between cell types ($p < 0.05$ for the third harmonics). Please note that the harmonics relative amplitude is an indication of the extent to which the cell behaves in a nonlinear manner; the larger the relative amplitude, the greater the cell response deviates from sinusoid. The actual values show that the GP myocytes are much more nonlinear than HEK cells, which is not surprising given the fact that only the former are capable of generating all-or-none action potentials. The values obtained in the LR2000 model are lower than those obtained from real cells, which may be attributable to the accuracy of the calcium cycling model.

In Fig. 9, we performed an additional analysis in GP cells to determine the underlying basis of the deviation from a sinusoidal response. Fig. 9, A and B, presents data at 10 Hz and 30 Hz, respectively. The upper graphs illustrate the voltage applied to the cell in a voltage-clamp experiment and the lower graph illustrates a family of currents analyzed in the experiment. First, we plotted total barium-sensitive current (*dotted line*) as the difference between currents recorded at 0 and 50 μM Ba^{2+}. Then, we estimated I_{K1} current as
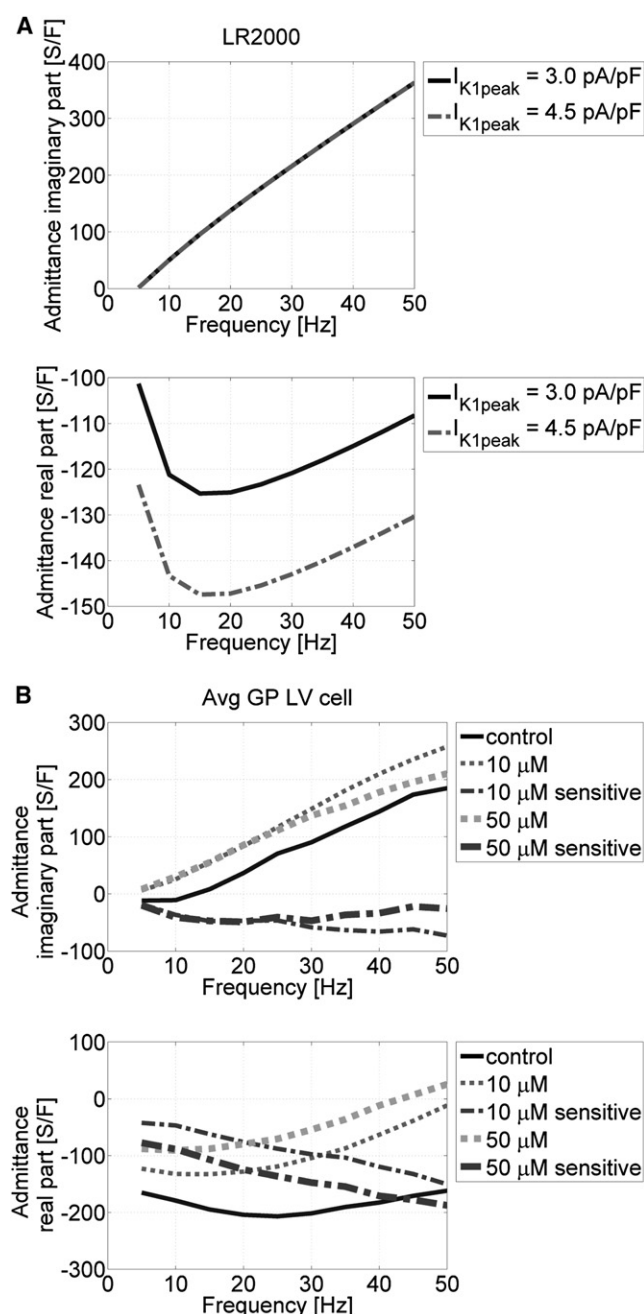
FIGURE 6 (A) Admittance characteristics in the LR2000 model, with solid lines representing admittance measured at $I_{K1peak} = 3.0$ pA/pF, and dash-dotted lines admittance at $I_{K1peak} = 4.5$ pA/pF. (B) Mean admittance characteristics in an average GP left ventricular cell. Admittance was measured in control conditions (solid lines), and in the presence of 10 μM Ba^{2+} (thin dotted lines) and 50 μM Ba^{2+} (thick dotted lines). Admittance sensitive to 10 μM Ba^{2+} was calculated as the difference between control and 10 μM Ba^{2+} measurements (thin dash-dotted lines), and admittance sensitive to 50 μM Ba^{2+} as the difference between control and 50 μM Ba^{2+} (thick dash-dotted lines).

$$i_{K1}(t) = I_{K1,DC} + g_{K1} \times (V_m(t) - V_{DC}),$$

where $I_{K1,DC}$ is the barium-sensitive current at V_{DC} and g_{K1} is the barium-sensitive dynamic conductance over the sinu-
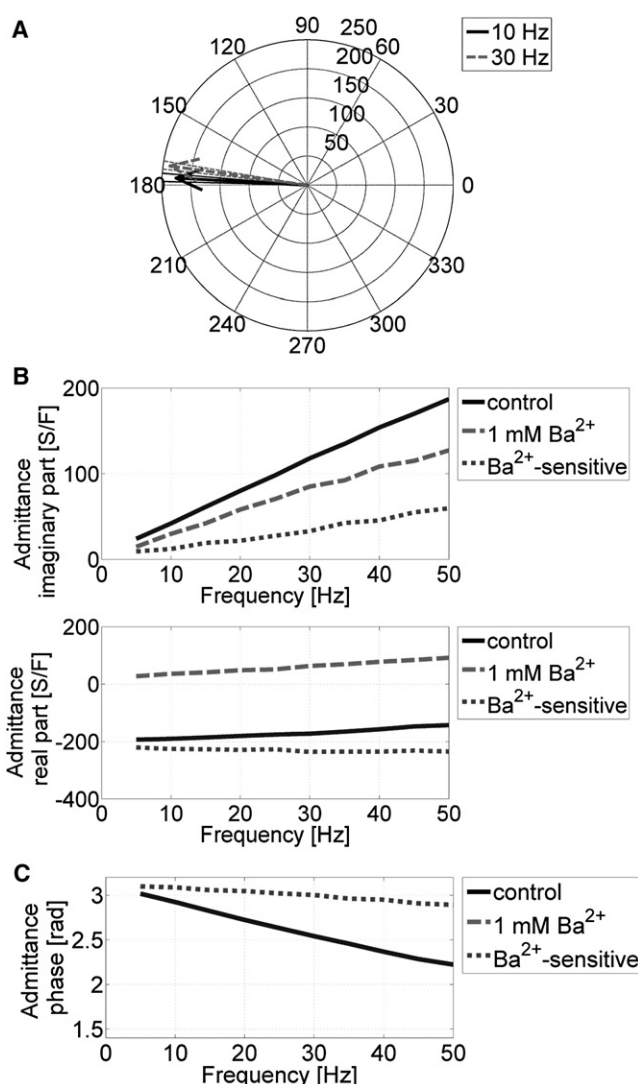

FIGURE 7 (A) Whole-cell Ba^{2+}-sensitive mean admittance in HEK cells at 1 mM (normalized to the cell capacitance and expressed in S/F), showing data at 10 Hz (solid lines) and 30 Hz (dashed lines). Vectors denote the mean, and radii denote the standard deviation calculated from admittances normalized to their magnitudes. (B and C) Average admittance characteristics as a function of frequency in HEK cells expressing Kir2.1/2.3 in control conditions (solid lines) and in the presence of 1 mM Ba^{2+} (dashed lines), as well as the Ba^{2+}-sensitive admittance, calculated as the vectorial difference between the control and 1 mM Ba^{2+} data (dotted lines; corresponding to the Ba^{2+}-sensitive current). (B) Imaginary (upper) and real (lower) parts of the admittance. (C) Argument (phase) of the admittance.

soidal voltage range (slope of the I/V, $\frac{di_{K1}}{dV_m}$). Both $I_{K1,DC}$ and g_{K1} were obtained specifically for every cell from ramp protocols run on that cell before and after the admittance protocol. Then, the estimated I_{K1} trace (dash-dotted line) was subtracted from the barium-sensitive current, and the difference was plotted (solid line) and referred to as "residual". Since this residual current could not be explained by the I_{K1} properties and was not observed in the HEK cell model, it must have a different ionic basis. The amplitude of the residual current in the presence of 50 μM
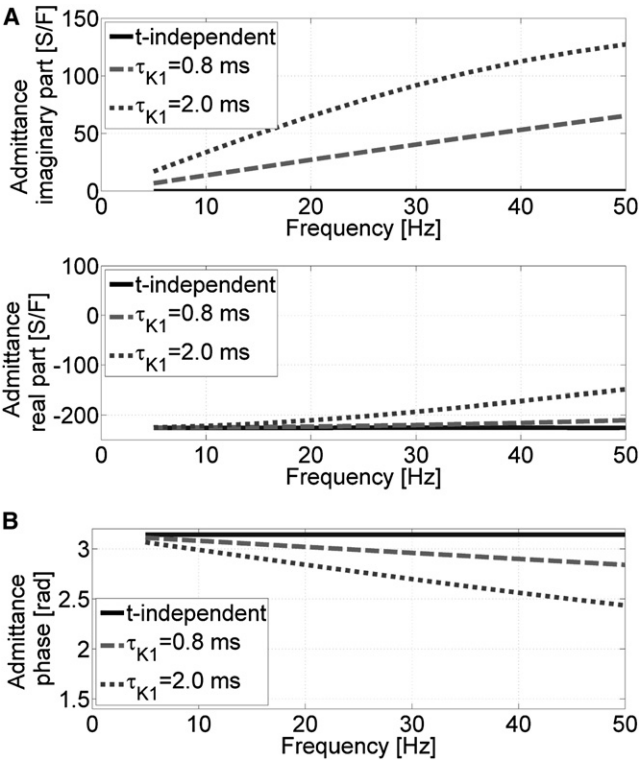
FIGURE 8 I_{K1} admittance in the LR2000 model (model equivalent of Ba^{2+}-sensitive admittance), calculated from three different time constants for I_{K1}. (A) Imaginary and real parts as a function of frequency. (B) Admittance phase as a function of frequency.

Ba^{2+} was -2316 ± 2371 pA at 10 Hz and -1477 ± 1270 pA at 30 Hz, ($n = 10$, $p < 0.05$). We hypothesized that the residual current was attributable to the L-type calcium channel. Given that the residual current is the component of Ba^{2+}-sensitive current, this explanation seems counterintuitive. Since it is known that Ba^{2+} can flow through L-type calcium channels, we could expect that adding Ba^{2+} to the solution would enhance I_{CaL} rather than block it. However, our explanation is in perfect agreement with the work by Fedida et al. (21), who measured the peak amplitude of inward current flowing through L-type calcium channels using square pulses to -10 mV from a holding potential of -40 mV. After replacement of extracellular calcium with barium, Fedida et al. (21) showed that the amplitude of the inward current was paradoxically reduced. In Fig. 10, we present the L-type calcium current flowing in response to sinusoidal voltages at 10 Hz in a computational single-cell model. As can be seen by comparing with Fig. 9 A, the shapes of I_{CaL} in the computer

TABLE 2   Relative harmonics levels in the current signal recorded

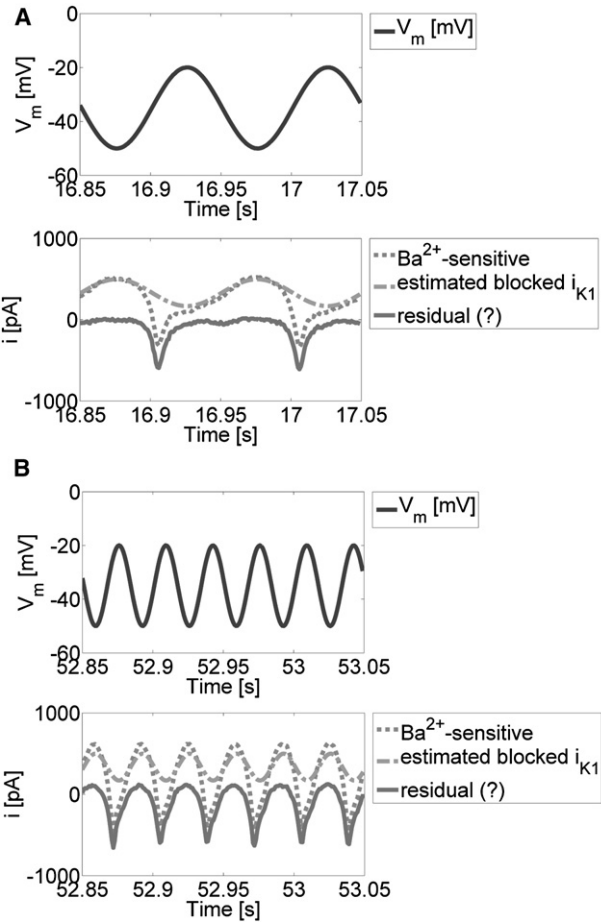| Cell	Relative second harmonics level at 10 Hz (pA/pA)	Relative third harmonics level at 10 Hz (pA/pA)
GP LV	0.45 ± 0.38	0.40 ± 0.34
HEK	0.21 ± 0.29	0.05 ± 0.04
LR2000	0.26	0.06

FIGURE 9   Analysis of the residual current in a representative guinea pig left ventricular cardiomyocyte at 10 Hz (A) and 30 Hz (B). Upper panels show the applied command voltage and lower panels the transmembrane currents: the barium-sensitive current (*dotted lines*), calculated as the difference between currents recorded at 0 and 50 μM Ba^{2+}; the theoretically estimated blocked (barium-sensitive) portion of the I_{K1} current (*dash-dotted lines*); and the residual difference between the total barium-sensitive current and the estimated blocked I_{K1} (*solid lines*).

simulation and the residual current in the real experiment are qualitatively similar; both have the shape of inward peaks. No other current (I_{NA}, I_{Kr}, I_{Ks}, I_{K1}, etc.) in the simulation is of similar shape or order of magnitude (data not shown). Moreover, the reduction of residual current amplitude observed in our experiments when frequency increased from 10 to 30 Hz is consistent with the kinetic characteristics of L-type calcium channel activation and deactivation.

Mechanistic insight

To provide a better insight into the mechanism of the observed relationship between single-cell and whole reentry properties, we plotted in Fig. 11 A a map of radial current for the simulation with $I_{K1peak} = 4.5$ pA/pF, as was done in Fig. 1 C for $I_{K1peak} = 3.0$ pA/pF. A brief glance at both maps reveals that the ''yin-yang'' pattern differs between the two cores; the isoline separating the blue and red regions
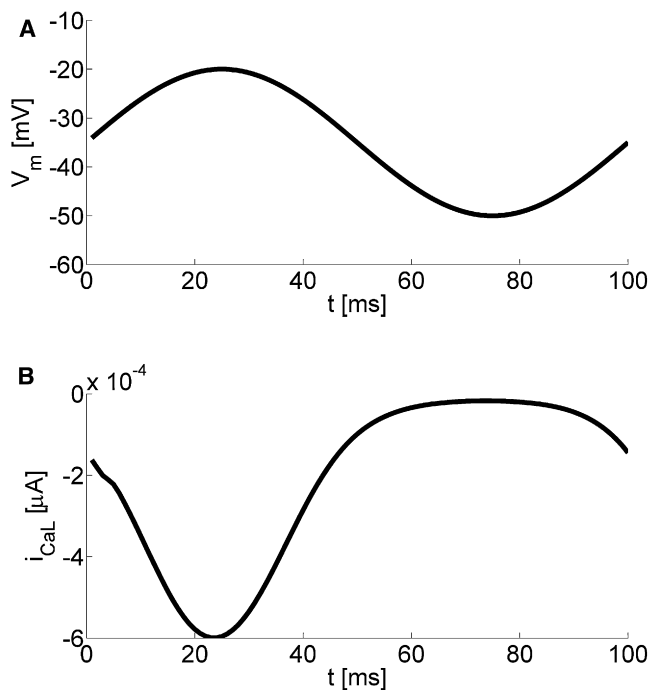
FIGURE 10 L-type calcium current in the simulated voltage-clamp experiment at a frequency of 10 Hz, showing the applied transmembrane voltage (A) and the current recorded in response (B).
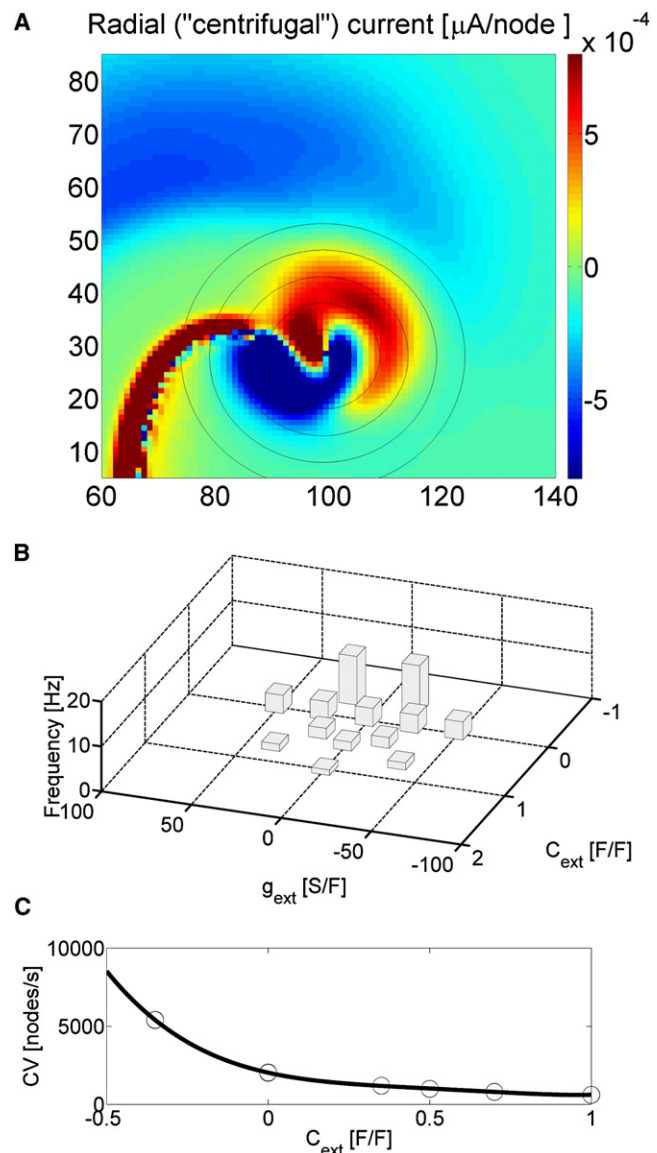

FIGURE 11 (A) Map of the radial current from the simulation with $I_{K1peak} = 4.5$ pA/pF, built analogously to the map in Fig. 1 C. (B) The frequency response of a 1D ring reentry as a function of external capacitance, C_{ext}, and conductance, g_{ext}, connected to each node. Both values are presented as normalized to the cell capacitance. (C) Conduction velocity in a 1D ring as a function of external capacitance. Circles denote data points from B and the solid line denotes the fourth-degree polynomial fit.

of the opposite current directions is more "twisted" in Fig. 11 A than in Fig. 1 C, which indicates that when there is a higher expression level of I_{K1}, the core provides electrotonic current to the surrounding tissue at different timing.

To analyze the electrotonic effects of the core on the wavefront traveling around it, we performed additional simulations. We simulated a reentry in a 1D ring composed of $L = 500$ nodes, using the LR2000 model at two different I_{K1} expression levels (3.0 and 4.5 pA/pF). The reentry parameters are shown in Table 3. The reduction in I_{K1} expression slightly increased the frequency and conduction velocity, which is the opposite of the findings in the 2D model. This indicates in turn that I_{K1} properties in the positive slope region (around the resting membrane potential) do not control rotor frequency, a result that justifies our decision to perform voltage-clamp measurements in the region of negative I/V slope.

We next investigated the effect of attaching an external capacitance (C_{ext}) and conductance (g_{ext}) to each cell in the ring (i.e., both C_{ext} and g_{ext} were connected in parallel to each other and in parallel to the cell capacitance and membrane currents). Fig. 11, B and C, shows the results of these simulations calculated for several values of C_{ext} and g_{ext}. It can be seen in Fig. 11 B that the frequency does not depend on the conductance, g_{ext}, but on the capacitance, C_{ext}. This relationship is clearly depicted in Fig. 11 C, where the frequency of reentry decreases as C_{ext} increases. This is not surprising, since the increase of external capacitance is equivalent to a reduction in sodium current.

From the physical viewpoint, the external capacitance connected to the cell acts as a sink when the transmembrane voltage is rising, thus dissipating the depolarizing current and slowing the conduction velocity. During repolarization, when the voltage is dropping, the capacitance would act as a current source, counteracting the repolarizing current. The interpretation of negative capacitance is the opposite: during the action potential upstroke, it would act as a current source, thus providing depolarizing current to the wavefront and facilitating propagation. During the repolarization phase, negative capacitance would act as a current sink, helping

TABLE 3 Parameters of reentry in a 1D ring composed of $L = 500$ (250) nodes

I_{K1peak}(pA/pF)	3.0	4.5
Reentry period (ms)	245.6 (125.6)	256.6 (129.4)
Reentry frequency (Hz)	4.072 (7.962)	3.897 (7.728)
Conduction velocity (nodes/s)	2036 (1990)	1949 (1932)

the cell to repolarize and shortening the action potential duration.

Data presented in Fig. 11, B and C, can be fitted using a fourth-degree polynomial:

$$CV = p_0 + p_1 C_{ext} + p_2 C_{ext}^2 + p_3 C_{ext}^3 + p_4 C_{ext}^4, \quad (3)$$

where $p_0 = 2027$, $p_1 = -4614$, $p_2 = 9703$, $p_3 = -11618$, and $p_4 = 5111$.

We then calculated the admittance of the core, as seen from its perimeter (and normalized to the perimeter length) at the different distance, r, from the center. These calculations were made according to Eq. 8, presented in the Appendix. The results are presented in Fig. 12 A. In this graph, we show the core admittance calculated for altogether four values, Y_m, of single-cell admittance; those Y_m values were read from Fig. 6 A for both membrane kinetics and
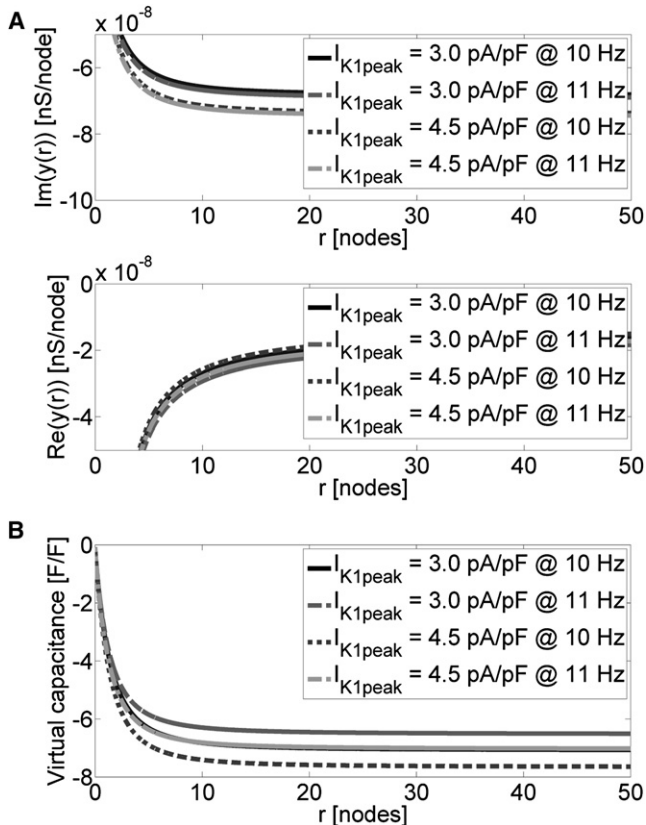

FIGURE 12 (A) Core admittance as seen from outside as a function of distance from the center, with both imaginary (*upper*) and real (*lower*) parts normalized to the perimeter length. (B) Virtual capacitance equivalent to the imaginary part of the core admittance.

two frequencies, 10 and 11 Hz. The results indicate that the core admittance imaginary part $Im[y(r)]$ reaches its steady-state value at as few as $r = 10$ nodes from the center. In the upper graph, one can see that the lines for $I_{K1peak} = 3.0$ pA/pF (*solid* and *dashed black lines*) at the two frequencies almost overlap. In a similar way, the two frequency lines for $I_{K1peak} = 4.5$ pA/pF (*dotted* and *dash-dotted gray lines*) almost overlap as well, but at different levels than in the case of $I_{K1peak} = 3.0$ pA/pF.

Thus, whereas I_{K1} modulation affects the real part of the single-cell admittance and leaves its imaginary part unaffected (as in Fig. 6 A), in the case of a multicellular core, the admittance imaginary part is the part most affected. Of course, the graph is meaningful only for r smaller than a core radius $R_{core} \approx 13$ nodes, and the remaining part is shown to document that the steady state is reached within the core radius, R_{core}.

We next converted the imaginary part of the core admittance to a corresponding "virtual capacitance" (C_{virt}) by dividing the imaginary part by $2\pi f$. The resulting dependence is shown in Fig. 12 B. It is not surprising that the virtual capacitance reaches its steady state at as few as $r = 10$ nodes from the center.

As the virtual core capacitance is negative, it indicates that the core would push the depolarizing electrotonic current to the wavefront and pull the repolarizing current from the wavetail. An increase in I_{K1} density exacerbates the core effect, whereas hypothetical reduction of rotor frequency would force the core to increase its effect.

DISCUSSION

We have used a combination of computer simulations and patch-clamp experiments in GP myocytes and HEK cells to investigate the relationship between the I_{K1}-induced changes in single-cell properties and the Ba^{2+}-induced changes in VF frequency in the whole heart. We have defined a new electrophysiological parameter, the single-cell frequency shift (Δf_{cell}), and also demonstrated that under certain conditions, the response of this parameter to I_{K1} blockade is like that of VF frequency.

Predictive value of the single-cell model

Our investigations have enabled us to develop a model suitable to quantitatively predict the effect of I_{K1} blockade on VF frequency change from measurements performed in a single cell. We hypothesized that when the rotation frequency changes due to Ba^{2+} application, the admittance phase measured using the approach specified in Methods remains constant. This hypothesis is equivalent to the expectation that the frequency shift, Δf_{cell}, in a single cell is approximately equal to the frequency shift, Δf_{rotor}, in a 2D or 3D system, in other words, that the ratio between those shifts should equal ~1:

$$\frac{\Delta f_{rotor}}{\Delta f_{cell}} \approx 1. \quad (4)$$

In our 2D simulations, this ratio between the frequency shift in the 2D rotor and the frequency shift in the single-cell model was $\frac{-1.17\ \text{Hz}}{-1.24\ \text{Hz}} = 0.94$, which is close to 1. This result demonstrates that by measuring in a single cell the frequency shift (Δf_{cell}) caused by I_{K1} blockade, we are able to predict, with reasonably good approximation, the consequences of such a blockade on the rotation frequency. The minimum discrepancy could be attributed to assumptions and simplifications made during our attempt to reproduce in single-cell simulations the conditions that prevail in the center of rotation during reentry in 2D.

Moreover, as shown in Figs. 5 and 7 of Warren et al. (2), the VF frequency in the intact GP heart decreased from ~30 Hz in control to ~18 Hz ($\Delta f_{\text{rotor}} = -12\ \text{Hz}$) and 12 Hz ($\Delta f_{\text{rotor}} = -18\ \text{Hz}$) in the presence of 10 and 50 μM Ba^{2+}, respectively. In our patch-clamp experiments, we obtained two significantly different values for Δf_{cell} at the two barium concentrations, and the ratio $\frac{\Delta f_{\text{rotor}}}{\Delta f_{\text{cell}}}$ was $\frac{-12\ \text{Hz}}{-14.14\ \text{Hz}} = 0.85$ and $\frac{-18\ \text{Hz}}{-18.51\ \text{Hz}} = 0.97$ for 10 and 50 μM Ba^{2+}, respectively (see Fig. 4 C).

Barium-sensitive current/admittance

As stated above, we had expected the Ba^{2+}-sensitive admittance to have a negative real part, a zero-value imaginary part, and, consequently, a phase of $\pm\pi$ rad. This expectation was based on 1), the fact that our measurements were done in the region of negative slope of the I_{K1} I/V profile; 2), the simplifying assumption that I_{K1} is an instantaneous current; and 3), the assumption that no other currents are affected by barium. However, in our experiments in HEK cells, we found that the phase of Ba^{2+}-sensitive admittance was slightly lower than π rad and decreased with increasing frequency. The apparent discrepancy between theoretical expectations and experimental results can, however, be reasonably explained by some time dependence of I_{K1}. A delay of the current response of the order of 1 ms (22) would correspond to a delay of 0.0628 rad at 10 Hz (vs. 0.0536 rad shown in Fig. 7 C), and of 0.1884 rad at 30 Hz (vs. 0.1386 rad shown in Fig. 7 C). Introduction of I_{K1} time dependence into the model confirmed that indeed time dependence is likely to be the mechanism of the aforementioned discrepancy. This result also demonstrates that our experimental sinusoidal voltage-clamp protocol was sensitive enough to detect time-dependent properties of the inward rectifier current, which are usually not visible in the standard voltage-clamp ramp protocol.

We have also found that Ba^{2+}-sensitive admittance (and thus the current flowing due to that admittance) in GP cells deviates much more from our theoretical prediction, and this discrepancy cannot be attributed to I_{K1} time dependence. In fact, whereas Ba^{2+}-sensitive admittance had a slightly positive imaginary part in HEK cells, there was a significant negative imaginary part in GP cells. Since we have found a good agreement between I_{K1} in HEK cells and its instantaneous model, we were able to subtract the I_{K1} estimate from

the Ba^{2+}-sensitive current, obtaining a residual Ba^{2+}-sensitive current, which was different from I_{K1}. Based on its time course and kinetic properties, we ascribed this current to the L-type calcium channel. However, there is a remaining discrepancy between 1), the flat course of the real part of the model equivalent of "Ba^{2+}-sensitive" admittance; and 2), the real part of true Ba^{2+}-sensitive admittance in GP myocytes, which in turn is frequency-dependent (Fig. 6). This discrepancy would be attributable to the fact that the model was not built to include the frequency dependence of the amplitude of I_{CaL}. However, a detailed investigation of this residual component will be carried out in a later study.

Mechanistic insight

In the Results section, we have developed two relationships. The first relationship describes how the electrotonic effect of the core (represented by C_{virt} and C_{ext}) depends on the rotation frequency during reentry and may be expressed by the equation

$$C_{\text{ext}} = \frac{\gamma}{2\pi \times f_{\text{rotor}}} \times \text{Im}\left(\pm \sqrt{\frac{\sigma Y_m}{\beta}} \right)$$

or, equivalently,

$$f_{\text{rotor}} = \frac{\gamma}{2\pi C_{\text{ext}}} \times \text{Im}\left(\pm \sqrt{\frac{\sigma Y_m}{\beta}} \right) \tag{5}$$

(see Eq. 9 in the Appendix and Fig. 12); it is noteworthy that this equation was based indeed on basic electricity laws (Ohm's, Kirchhoff's, etc.).

Now we can refer back to Fig. 11 C, which describes electrophysiological properties of the cells, and calculate the tangential component of conduction velocity at the perimeter core as

$$CV_t = CV_\infty \times \kappa \times \cos(\alpha),$$

where CV_∞ is the conduction velocity of a planar wave from Fig. 11 C, κ counts for CV reduction due to wavefront curvature, and α denotes the angle between the conduction velocity vector and the tangent to the core. Given that

$$CV_t = 2\pi R_{\text{core}} \times f_{\text{rotor}}$$

and using polynomial approximation of the relationship from Fig. 11 C, we obtain

$$f_{\text{rotor}} = \frac{\kappa \times \cos(\alpha)}{2\pi R_{\text{core}}} \times \left(p_0 + p_1 C_{\text{ext}} + p_2 C_{\text{ext}}^2 + p_3 C_{\text{ext}}^3 + p_4 C_{\text{ext}}^4 \right). \tag{6}$$

Combining Eqs. 5 and 6, we obtain

$$f_{\text{rotor}} = \frac{\gamma}{2\pi C_{\text{ext}}} \times \text{Im}\left(\pm \sqrt{\frac{\sigma Y_m}{\beta}} \right) = \frac{\kappa \times \cos(\alpha)}{2\pi R_{\text{core}}} \cdot \left(p_0 + p_1 C_{\text{ext}} + p_2 C_{\text{ext}}^2 + p_3 C_{\text{ext}}^3 + p_4 C_{\text{ext}}^4 \right), \tag{7}$$

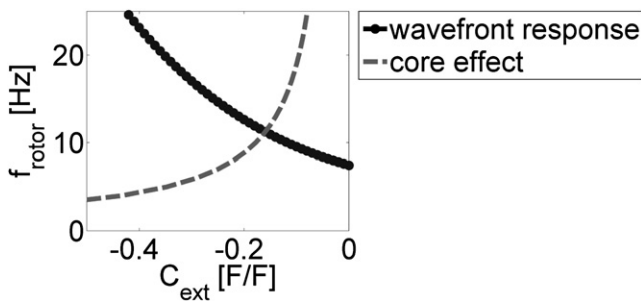which would determine the rotation frequency of the reentry.

FIGURE 13 Model of the core-wavefront interaction. The chain of solid circles shows the effect of "core capacitance" (C_{ext}) on the frequency of the wavefront rotating around it. This relationship was derived from Fig. 11 C and Eq. 6 using the scaling coefficient $\kappa \times \cos(a) = 0.3$. The dashed line shows how the "core capacitance" seen from outside depends on the frequency of rotation (independent variable is on the vertical axis!); this relationship was obtained from Eq. 5 using the scaling coefficient $\gamma = 0.025$ and $Y_m \approx (-120 + 2\pi f \times j)$ F/F (for $I_{K1peak} = 3.0$ pA/pF). Please note that scaling coefficients were selected arbitrarily within a reasonable range, as the collected data was not sufficient to calibrate them.

However, Y_m has built-in dependence on frequency (see Fig. 4 A). For the purpose of graphical presentation, we approximated $Y_m \approx (-120 + 2\pi f \times j)$ F/F. Next, we plotted Eqs. 5 and 6 (Fig. 13). Since the collected data were not sufficient to estimate scaling factors that appear in the equations, we had to select arbitrarily some reasonable values. Thus, the figure is useful to explain the mechanism of frequency control but does not allow determination of its absolute value.

In the example, the reentry frequency would be ~11 Hz. If, for any reason, the reentry was rotating faster (say, at 20 Hz), then the electrotonic effect of the core (as measured by $C_{ext} = -0.1$ at 20 Hz (Fig. 13, dashed line)) would be sufficient to keep the wavefront rotating only at 9 Hz (solid line), and reentry would have to slow down. On the other hand, if for any reason reentry was rotating more slowly (say, at 5 Hz), then the electrotonic effect of the core (as measured by $C_{ext} = -0.35$ at 5 Hz (Fig. 13, dashed line)) would be strong enough to speed up reentry to 20 Hz, and reentry would have to speed up.

This feedback mechanism will bring the rotor frequency to the frequency at the intersection of the solid and dashed lines in Fig. 13 and should be responsible for keeping the admittance phase at a constant level; the strength of the feedback would account for the deviation of $\frac{\Delta f_{rotor}}{\Delta f_{cell}}$ from 1. Also, the feedback strength would be responsible for the phase-locking behavior of the whole 2D reentry.

Limitations

It is noteworthy that the reentry frequency in our 2D simulation deviates from the values observed by Warren et al. (2) in the intact GP heart. This discrepancy can be partially attributed to the accuracy of the kinetics of the model: the LR2000 model is for a "general" ventricular cell and the rotation frequency value in the intact heart was recorded in the left

ventricle, since the frequency in the right ventricle is much slower, i.e., of the order of 10 Hz. Moreover, reentry in the intact heart occurs in a complex 3D structure with epicardial-endocardial gradients and rotational anisotropy (23). However, even though absolute rotor frequencies differ between the experiments of Warren et al. (2) and our 2D simulations, the response to barium fulfills the condition $\frac{\Delta f_{rotor}}{\Delta f_{cell}} \approx 1$ (0.8 ≈ 1). This result therefore allowed us to quantitatively predict the frequency of VF based on the electrophysiological properties of a single-cell model.

The presence of EGTA in the pipette, which was necessary to make the cells survive the protocol, is also a potential limiting factor.

The proposed explanation of the observed reentry behavior depends on several assumptions of homogeneity of admittance properties of the cells within the core and reentry parameters, such as core diameter not varying because of I_{K1} modulation. Furthermore, we assumed that the rotor was stable. Since rotors in VF are often unstable, especially when restitution of the action potential duration is steep, one must be careful when attempting to extrapolate the results from the guinea pig to other species. In addition to drifting and meandering, other properties of rotor behavior (including wavebreaks away from the core) may be important but are out of the scope of the theory presented here.

Several studies have dealt with the effect of specific ionic currents on the behavior of rotors (4); however, to our knowledge, no mathematical formulation describing the electrical behavior of the reentry core has been presented. In our first attempt to develop such a description, we have made several assumptions and approximations on the core parameter stability, homogeneity of core properties, periodicity, etc. Therefore, several important ionic mechanisms involved in the reentry behavior were not considered in this work. These currents will be incorporated in a later study.

Whereas the conditions in the core vary with the distance, ranging from an almost flat voltage trace at the center, through sinusoids of increasing amplitude, to various action potential shapes, a question may arise regarding which voltage shape should be used to investigate the properties and behavior of the cells within the core. Application of all voltage traces present at different distances from the core center is impractical. Therefore, we were forced to select a trace that would be representative of core conditions. In this study, we were interested in measuring admittance of the cells. As already mentioned in relation to Fig. 1, the behavior of the core within a five-node radius is linear. Also, at 15 nodes from the center, both current and voltage courses (Fig. 1, B and D) are the same shape, indicating that even though both signals contain harmonic components, the core behaves in a fairly linear fashion. This suggests that there is a relatively homogeneous distribution of cell admittance within the core, which justifies our seemingly arbitrary reference to the voltage five nodes from the center.

As can be inferred from Fig. 1, at greater distances from the core, for example, ~13–15 nodes from the center, two phenomena coincide: 1), wavefront propagation associated with large electrotonic depolarizing current due to sodium channels begins; and 2), the region of negative I/V slope is left behind. In the context of the theory presented here, the presence of significant regions with both positive and negative I_{K1} slopes within the core would make the analysis of the core admittance more complicated (see Eq. 8).

Even considering that the proposed protocol does not exactly reproduce the core condition, it is important to notice that our protocol at least approximates conditions experienced by the ion channels in the core. As shown by Millonas and Hanck (24), and by Kargol et al. (25), the ionic current properties observed in the context of constantly alternating voltage may differ from those visible in classical ramp or step protocols.

It is also noteworthy that the voltage-clamp protocol applied in silico or in vitro to a single cell is only an approximation of the conditions in the core, given that the conditions therein are not ideally homogenous (see Fig. 1 for comparison). Finally, another potential limitation arises from the fact that we investigated the role of I_{K1} only, as the major contributor to rotation frequency control. Our intention in doing so was to focus only on the repolarizing potassium current, which significantly affects rotation frequency and activates the conditions present in the core.

Despite these limitations, our results demonstrate the usefulness of the single-cell model in predicting VF behavior in the whole heart.

APPENDIX

Let us consider the behavior of the core of the reentry, rotating at some frequency, f_{rotor}, as presented in Fig. 1, i.e. the behavior of model tissue within the distance $R_{\text{core}} = 13$ nodes from the center. Let us assume that the admittance of each cell (normalized to capacitance) in the core equals Y_m. In a polar coordinate system, let $V(r, \theta)$, $I_r(r, \theta)$, and $I_t(r, \theta)$ denote the spatial distribution of complex representations (phasors) of transmembrane voltage (Fig. 1 A), radial current density (Fig. 1 C), and tangential current density, respectively.

Because of the periodicity, the transmembrane voltage distribution can be written as

$$V(r, \theta) = V(r) \times \exp(j\theta).$$

Then, the radial current density is

$$I_r(r, \theta) = -\sigma \frac{\partial V(r, \theta)}{\partial r} = -\sigma V'(r) \times \exp(j\theta)$$

and the tangential counterclockwise current density is

$$I_t(r, \theta) = -\sigma \frac{\partial V(r, \theta)}{r \times \partial \theta} = -\sigma \frac{V(r)}{r} \times j \times \exp(j\theta)$$
$$= -j\sigma \frac{V(r)}{r} \times \exp(j\theta).$$

As the total transmembrane current and current divergence sum up to 0,

$$\frac{\partial (rI_r(r, \theta))}{r \times \partial r} + \frac{\partial I_t(r, \theta)}{r \times \partial \theta} + \beta Y_m \times V(r, \theta) = 0,$$

we can write

$$-\beta Y_m \times V(r, \theta) = \frac{\partial (rI_r(r, \theta))}{r \times \partial r} + \frac{\partial I_t(r, \theta)}{r \times \partial \theta}$$
$$= \frac{\partial (-\sigma \times r \times V'(r) \times \exp(j\theta))}{r \times \partial r}$$
$$+ \frac{\partial \left(-j\sigma \frac{V(r)}{r} \times \exp(j\theta)\right)}{r \times \partial \theta}$$

$$-\beta Y_m \times V(r) \times \exp(j\theta) = -\sigma \times V''(r) \times \exp(j\theta)$$
$$- \sigma \frac{V'(r)}{r} \times \exp(j\theta)$$
$$- j^2 \sigma \frac{V(r)}{r^2} \times \exp(j\theta)$$

$$-\beta Y_m \times V(r) = -\sigma V''(r) - \sigma \frac{V'(r)}{r} + \sigma \frac{V(r)}{r^2}$$

$$V''(r) = V(r) \left(\frac{1}{r^2} + \frac{\beta Y_m}{\sigma}\right) - \frac{V'(r)}{r}$$

$$\frac{V''(r)}{V(r)} = \left(\frac{1}{r^2} + \frac{\beta Y_m}{\sigma}\right) - \frac{1}{r} \times \frac{V'(r)}{V(r)}.$$

Recall that the radial current, described by the current density, $I_r(r, \theta)$, is the only current crossing the perimeter at distance r. In other words, the electrotonic effect exerted by the core area lying within some specific radius r on the surrounding tissue can be described by $I_r(r, \theta)$, which in turn depends on the voltage, $V(r, \theta)$, along the perimeter at radius r. Moreover, as long as the properties of the core can be approximated as linear, the relationship between $I_r(r, \theta)$ and $V(r, \theta)$ can be described with admittance of the core

$$y(r) = \frac{-I_r(r, \theta)}{V(r, \theta)} = -\frac{-\sigma V'(r) \times \exp(j\theta)}{V(r) \times \exp(j\theta)} = \frac{\sigma V'(r)}{V(r)}$$

where $y(r)$ is admittance of the core contained within radius r, normalized to the perimeter length. Therefore,

$$\frac{y'(r)}{\sigma} = \frac{V''(r)V(r) - V'(r) \cdot V'(r)}{V^2(r)} = \frac{V''(r)}{V(r)} - \left(\frac{V'(r)}{V(r)}\right)^2$$
$$= \frac{V''(r)}{V(r)} - \left(\frac{y(r)}{\sigma}\right)^2$$

and $y(r)$ must satisfy the differential equation

$$\frac{y'(r)}{\sigma} + \left(\frac{y(r)}{\sigma}\right)^2 = \frac{1}{r^2} + \frac{\beta Y_m}{\sigma} - \frac{1}{r} \times \left(\frac{y(r)}{\sigma}\right)$$

$$\frac{y'(r)}{\sigma} = \left(\frac{1}{r^2} + \frac{\beta Y_m}{\sigma}\right) - \left(\frac{y(r)}{\sigma}\right)^2 - \frac{1}{r} \times \left(\frac{y(r)}{\sigma}\right). \quad (8)$$

The latter is an example of Riccati's equation and has no known analytical solution except in some special cases. Therefore, we picked up Y_m

values from Fig. 6 A for both membrane and two frequencies (10 and 11 Hz) and solved Eq. 8 numerically using Euler's method.

Since $y(r)$ is not defined at $r = 0$, we also needed to select some initial conditions, $y_0 = y(r_0)$. Since $\lim_{r \to \infty} \frac{y(r)}{\sigma} = \sqrt{\frac{\beta Y_m}{\sigma}}$, we selected $r_0 = 1000$ and $\frac{y_0}{\sigma} = \sqrt{\frac{\beta Y_m}{\sigma}}$. The solution at a low range of r ($r \leq 50$) did not depend on the sign selection for y_0.

The results of $y(r)$ calculation are shown in Fig. 12 A. We then converted the imaginary part of the core admittance to a corresponding "virtual capacitance" by dividing the imaginary part over $2\pi f$ (Fig. 12 B). Consequently, we can conclude that each cell at the core perimeter (at R_{core} from the center) "feels" the core electrotonic influence as equivalent to a virtual capacitance

$$C_{virt} = \frac{Im\left(\pm \sqrt{\sigma \times \beta Y_m} \right)}{2\pi f_{rotor}}$$

connected to that cell (the notion of equivalency is limited, as C_{virt} would be frequency-dependent). As the cell at the core perimeter is also connected to the next more distant "rings" or "layers" of cells, the effect of the virtual capacitance, C_{virt}, would be spread out between those several layers. We will approximate it using some coefficient $0 \leq \gamma \leq 1$ (say, $\gamma = 0.1$ would mean that only 10% of the core's virtual-capacitance electrotonic input stays within the first layer of cells; indeed, γ will incorporate the space constant outside the core—the larger the space constant, the smaller the γ value):

$$C_{ext} = \frac{\gamma}{\beta} C_{virt};$$

the presence of β in the last equation relates to the fact that C_{virt} is expressed in farads/node and C_{ext} is normalized per cell capacitance (i.e., expressed in farads/farad).

Thus, we obtain the equation binding the core admittance properties and the frequency of the rotor

$$f_{rotor} = \frac{\gamma}{\beta} \times \frac{Im\left(\pm \sqrt{\sigma \times \beta Y_m} \right)}{2\pi C_{ext}}$$
$$= \frac{\gamma}{2\pi C_{ext}} \times Im\left(\pm \sqrt{\frac{\sigma Y_m}{\beta}} \right). \qquad (9)$$

SUPPORTING MATERIAL

Two movies are available at http://www.biophysj.org/biophysj/supplemental/S0006-3495(09)00386-5.

REFERENCES

1. Noujaim, S. F., S. V. Pandit, O. Berenfeld, K. Vikstrom, M. Cerrone, et al. 2007. Up-regulation of the inward rectifier K$^+$ current (I K1) in the mouse heart accelerates and stabilizes rotors. *J. Physiol.* 578:315–326.

2. Warren, M., P. K. Guha, O. Berenfeld, A. Zaitsev, J. M. Anumonwo, et al. 2003. Blockade of the inward rectifying potassium current terminates ventricular fibrillation in the guinea pig heart. *J. Cardiovasc. Electrophysiol.* 14:621–631.

3. Choi, B. R., T. Liu, and G. Salama. 2001. The distribution of refractory periods influences the dynamics of ventricular fibrillation. *Circ. Res.* 88:E49–E58.

4. Beaumont, J., N. Davidenko, J. M. Davidenko, and J. Jalife. 1998. Spiral waves in two-dimensional models of ventricular muscle: formation of a stationary core. *Biophys. J.* 75:1–14.

5. Choi, B. R., W. Nho, T. Liu, and G. Salama. 2002. Life span of ventricular fibrillation frequencies. *Circ. Res.* 91:339–345.

6. Muñoz, V., K. R. Grzęda, T. Desplantez, S. V. Pandit, S. Mironov, et al. 2007. Adenoviral expression of IKs contributes to wavebreak and fibrillatory conduction in neonatal rat ventricular cardiomyocyte monolayers. *Circ. Res.* 101:475–483.

7. Anumonwo, J. M., M. Delmar, A. Vinet, D. C. Michaels, and J. Jalife. 1991. Phase resetting and entrainment of pacemaker activity in single sinus nodal cells. *Circ. Res.* 68:1138–1153.

8. Banerjee, D. 2006. PLL Performance, Simulation and Design, 4th ed. Dog Ear, Indianapolis, IN.

9. Jalife, J. 1984. Mutual entrainment and electrical coupling as mechanisms for synchronous firing of rabbit sino-atrial pace-maker cells. *J. Physiol.* 356:221–243.

10. Michaels, D. C., E. P. Matyas, and J. Jalife. 1984. A mathematical model of the effects of acetylcholine pulses on sinoatrial pacemaker activity. *Circ. Res.* 55:89–101.

11. Winfree, A. T. 1967. Biological rhythms and the behavior of populations of coupled oscillators. *J. Theor. Biol.* 16:15–42.

12. Anumonwo, J. M., L. C. Freeman, W. M. Kwok, and R. S. Kass. 1992. Delayed rectification in single cells isolated from guinea pig sinoatrial node. *Am. J. Physiol.* 262:H921–H925.

13. Dhamoon, A. S., S. V. Pandit, F. Sarmast, K. R. Parisian, P. Guha, et al. 2004. Unique Kir2.x properties determine regional and species differences in the cardiac inward rectifier K$^+$ current. *Circ. Res.* 94:1332–1339.

14. Morley, G. E., J. M. Anumonwo, and M. Delmar. 1992. Effects of 2,4-dinitrophenol or low [ATP]i on cell excitability and action potential propagation in guinea pig ventricular myocytes. *Circ. Res.* 71:821–830.

15. Muñoz, V., R. Vaidyanathan, E. G. Tolkacheva, A. S. Dhamoon, S. M. Taffet, et al. 2007. Kir2.3 isoform confers pH sensitivity to heteromeric Kir2.1/Kir2.3 channels in HEK293 cells. *Heart Rhythm.* 4:487–496.

16. Chen W. -K., editor. 2006. Circuit Analysis and Feedback Amplifier Theory. CRC Press, Chicago. http://www.engnetbase.com/ejournals/books/book_summary/summary.asp?id=4593. Accessed March 4, 2009.

17. Faber, G. M., and Y. Rudy. 2000. Action potential and contractility changes in [Na(+)](i) overloaded cardiac myocytes: a simulation study. *Biophys. J.* 78:2392–2404.

18. Faber, G.M. The Luo-Rudy Dynamic (LRd) model of the mammalian ventricular action potential. http://www.cwru.edu/med/CBRTC/LRdOnline/LRdModel. Accessed March 4, 2009.

19. Czarnul, P., and K. Grzęda. 2004. Parallel simulations of electrophysiological phenomena in myocardium on large 32 and 64-bit Linux clusters. *EuroPVM/MPI Lect. Notes Comput. Sci.* 3241:234–241.

20. Samie, F. H., O. Berenfeld, J. M. Anumonwo, S. F. Mironov, S. Udassi, et al. 2001. Rectification of the background potassium current: a determinant of rotor dynamics in ventricular fibrillation. *Circ. Res.* 89:1216–1223.

21. Fedida, D., D. Noble, and A. J. Spindler. 1988. Mechanism of the use dependence of Ca^{2+} current in guinea-pig myocytes. *J. Physiol.* 405:461–475.

22. Lopatin, A. N., L. M. Shantz, C. A. Mackintosh, C. G. Nichols, and A. E. Pegg. 2000. Modulation of potassium channels in the hearts of transgenic and mutant mice with altered polyamine biosynthesis. *J. Mol. Cell. Cardiol.* 32:2007–2024.

23. Xie, F., Z. Qu, J. Yang, A. Baher, J. N. Weiss, et al. 2004. A simulation study of the effects of cardiac anatomy in ventricular fibrillation. *J. Clin. Invest.* 113:686–693.

24. Millonas, M. M., and D. A. Hanck. 1998. Nonequilibrium response spectroscopy of voltage-sensitive ion channel gating. *Biophys. J.* 74:210–229.

25. Kargol, A., A. Hosein-Sooklal, L. Constantin, and M. Przestalski. 2004. Application of oscillating potentials to the Shaker potassium channel. *Gen. Physiol. Biophys.* 23:53–75.